

# Quantum skyrmions in the antiferromagnetic triangular lattice

Inés Corte<sup>1,2</sup> \* Federico Holik<sup>1</sup>, Lorena Rebon<sup>1,2</sup>, and Flavia A. Gómez Albarracín<sup>3,2</sup>

<sup>1</sup>*Instituto de Física La Plata (CONICET-UNLP). Diagonal 115 S/N, La Plata, Argentina.*

<sup>2</sup>*Departamento de Ciencias Básicas, Facultad de Ingeniería,*

*Universidad Nacional de La Plata (UNLP). Avenida 1 y 47 S/N, La Plata, Argentina. and*

<sup>3</sup>*Instituto de Física de Líquidos y Sistemas Biológicos (CONICET-UNLP). Calle 59 789, La Plata, Argentina*

(Dated: January 27, 2026)

Magnetic skyrmions are topological quasiparticles potentially useful for memory and computing devices. Antiferromagnetic (AF) skyrmions present no transverse deflection, making them suitable candidates for data storage applications. After the discovery of skyrmions with length scales comparable to the lattice constant, several works presented quantum analogues of classical ferromagnetic skyrmions in spin systems. However, studies about quantum analogues of AF skyrmions are still lacking. Here, we explore the phases of the AF quantum spin-1/2 Heisenberg model with Dzyaloshinskii-Moriya interactions on the triangular lattice using the density matrix renormalization group (DMRG) algorithm. We study the magnetization profile, spin structure factor and quantum entanglement of the resulting ground states to characterize the corresponding phases and signal the emergence of quantum AF skyrmions. Our results support that three-sublattice quantum antiferromagnetic skyrmion textures are stabilized in a wide range of magnetic fields.

## I. Introduction

Magnetic skyrmions are swirling magnetic textures [1, 2] characterized by a non-trivial topological invariant in real space called topological charge and defined as

$$N_{Sk} = \frac{1}{4\pi} \int d^2x \mathbf{m}(\mathbf{r}) \cdot (\partial_x \mathbf{m}(\mathbf{r}) \times \partial_y \mathbf{m}(\mathbf{r})), \quad (1)$$

where  $\mathbf{m}(\mathbf{r})$  is a local unit vector field associated to the spin vector at position  $\mathbf{r}$ . The topological charge  $N_{Sk}$  counts how many times the texture wraps around a sphere, and it yields  $|N_{Sk}| = 1$  for skyrmions.

Due to their non-trivial topology, skyrmions are robust spin textures and have therefore attracted considerable attention, particularly in connection with potential technological applications such as memory devices [3–5]. These textures may be physically stabilized via different mechanisms [6], ranging from magnetic frustration [7–9] to long-range interactions [10]. One of the most relevant mechanisms to realize skyrmions in non-centrosymmetric systems is the in-plane Dzyaloshinskii-Moriya interaction (DMI), a key ingredient in the models connected to the first experimental measurements [11, 12].

Skyrmions usually encountered in experimental measurements behave like classical particles. However, their size can range from micrometers to lengths comparable to the interatomic lattice spacing. Since quantum effects can play an important role in the latter case, skyrmions with diameters of a few nanometers may not be well-described using classical spins. Several numerical studies of quantum analogs of ferromagnetic (F) skyrmions have been made over recent years [13–19]. These works state the emergence of quantum ferromagnetic skyrmions as

ground states of model Hamiltonians using spin waves [13], exact diagonalization [14–16], neural network quantum states [17, 18] and density matrix renormalization group (DMRG) methods [19]. Most importantly, different measures of quantum entanglement between spins show that these ferromagnetic skyrmion states present entanglement [16, 17, 19] and hence are indeed truly quantum. In this work, we focus instead on quantum properties of antiferromagnetic (AF) skyrmions.

One of the possible issues that may arise when considering technological applications is the so-called skyrmion Hall effect, which is the deviation of skyrmions when driven by a current. Different topological quasiparticles have been proposed as suitable candidates where this effect may be suppressed. Among them, of particular interest are the antiferromagnetic skyrmions, which have been recently observed in a number of materials [20–24]. Quantum effects in these textures have been studied using techniques such as spin waves [25] and a modified quantum Monte Carlo method [26]. In this work, we explore the magnetic phases of ground states for a simple skyrmion Hamiltonian in the antiferromagnetic triangular lattice with  $S = 1/2$  spins obtained using the DMRG algorithm [27–29]. Although originally developed for one-dimensional quantum systems, this method has proven to be a powerful tool to compute ground states of two-dimensional lattices [30–34]. In particular, DMRG was recently used to successfully simulate ground states hosting quantum ferromagnetic skyrmions [19, 34]. Here, we follow a similar approach, showing evidence of the formation of skyrmions in the AF triangular lattice upon an external magnetic field and studying quantum effects such as the entanglement.

This article is organized as follows. In Section II, we specify the model Hamiltonian used in the DMRG calculations. This Hamiltonian gives rise to AF skyrmions in a classical-spins scenario. Our numerical findings are discussed in Section III, where we argue the emergence

\* corresponding author: ines.corte@iflp.unlp.edu.ar

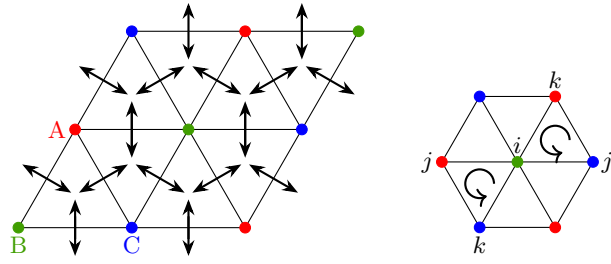


FIG. 1. Left: Sites that belong to each of the three sublattices of the triangular lattice, where “A”, “B”, “C” label spin sites in each of the sublattices. Sites having the same color form part of the same sublattice. Arrows indicate the directions of the DMI vectors  $\mathbf{D}_{\mathbf{r}',\mathbf{r}}$ . Right: Two representative sets of sites  $(i, j, k)$  used to compute the chirality in Eq.(4). We label the sites of the vertices of each triangular plaquette as  $i, j$  and  $k$  following a counterclockwise order. Note that each site belongs to a different sublattice.

of quantum AF skyrmions as our main result. We calculate the magnetization and magnetic susceptibility (Section III A), analyze the chirality (Section III B) and compute the structure factor (Section III C) of the ground states found with DMRG. We also inspect whether the AF skyrmion texture is influenced by the boundary shape and lattice size in Section III D. Additionally, we employ entanglement measures to characterize the AF skyrmion phase in Section III E. To conclude, we summarize our results in Section IV.

## II. Model and methods

The main goal of this work is to study the possible stabilization of skyrmions for  $S = 1/2$  spins in an antiferromagnetic model. To this end, we study the two-dimensional spin-1/2 Heisenberg model with DMI and antiferromagnetic exchange couplings  $J > 0$  in the triangular lattice. We employ the Hamiltonian

$$\hat{H} = \sum_{\langle \mathbf{r}, \mathbf{r}' \rangle} [J \hat{\mathbf{S}}_{\mathbf{r}} \cdot \hat{\mathbf{S}}_{\mathbf{r}'} + \mathbf{D}_{\mathbf{r}',\mathbf{r}} \cdot (\hat{\mathbf{S}}_{\mathbf{r}} \times \hat{\mathbf{S}}_{\mathbf{r}'}))] - \sum_{\mathbf{r}} B \hat{\mathbf{z}} \cdot \hat{\mathbf{S}}_{\mathbf{r}}, \quad (2)$$

where  $\hat{\mathbf{S}}_{\mathbf{r}} = (\hat{S}_{\mathbf{r}}^x, \hat{S}_{\mathbf{r}}^y, \hat{S}_{\mathbf{r}}^z)$  ( $\hat{S}_{\mathbf{r}}^{\alpha}$  with  $\alpha = x, y, z$  are spin operators acting at position  $\mathbf{r}$ ),  $\mathbf{D}_{\mathbf{r}',\mathbf{r}} = D \hat{\mathbf{z}} \times (\mathbf{r}' - \mathbf{r}) / |\mathbf{r}' - \mathbf{r}|$  is the in-plane DMI with strength  $D$  between nearest-neighbor lattice sites at positions  $\mathbf{r}$  and  $\mathbf{r}'$ , and  $B$  is the external magnetic field perpendicular to the plane. In addition, the first summation runs over all unique nearest-neighbor spin pairs. We fix  $J = 1$  so that  $J$  sets the energy scale throughout the rest of this article.

The classical counterpart of the Hamiltonian from Eq.(2) exhibits an antiferromagnetic skyrmion lattice phase, stabilized in a broad range of temperatures and intermediate magnetic fields [35, 36]. This phase is formed by three interpenetrated ferromagnetic skyrmion lattices,

one in each sublattice of the triangular lattice (sublattices defined in Fig. 1). This type of texture has been shown to be experimentally relevant to  $\text{MnSc}_2\text{S}_4$  [20, 21] and similar phases are known to arise in other frustrated models [37–39]. At lower fields, interpenetrated helices form an antiferromagnetic helices pattern, which leads to the antiferromagnetic skyrmion lattice as the magnetic field is increased. For larger magnetic fields, intermediate skyrmion-like textures arise before reaching saturation.

In the present work, we take  $S = 1/2$  and resort to DMRG to study signatures of quantum antiferromagnetic skyrmions. We used the DMRG implementation from the ITensorMPS library, which is based on the Julia version of ITensor [40], to perform our calculations. See the Appendix A for information on convergence and technical details.

To analyze the ground states of  $\hat{H}$  from Eq.(2), we worked with lattices of  $N = L^2$  sites with  $L = 12, 20$  (unless stated otherwise), taking open boundary conditions (OBC) and fixing  $D/J = 0.8$ . We focus especially at intermediate magnetic fields, where skyrmion-hosting phases may arise. We find evidence of three-sublattice skyrmion textures for a wide range of magnetic fields and irrespective of how the boundaries of the lattice are chosen, as we will show in the next section. We also present magnetization profiles and compute the chirality, which is a quantized discrete version of the topological charge  $N_{Sk}$ . In classical systems, a non-zero chirality is associated with skyrmions. This has also been the case for quantum ferromagnetic skyrmions hosted in spin-1/2 systems [15]. In addition, we inspect the quantum entanglement of these antiferromagnetic textures, which is a strictly non-classical phenomenon. We discuss our findings in the next section.

## III. Results

As stated before, the main aim of this work is to identify the different emerging phases for the Hamiltonian in Eq.(2) for  $S = 1/2$  spins. For that purpose, we computed the magnetization and scalar chirality of the system and found three main phases: antiferromagnetic helical phases at lower fields, an intermediate antiferromagnetic skyrmion phase and finally, a fully polarized phase. As in the classical model, there is also an intermediate chiral phase as skyrmions become polarized and before the system goes into the ferromagnetic phase. We also explore the emergent skyrmion phase in reciprocal space calculating the structure factor. Furthermore, despite the expected boundary effects due to the system size and OBC, we show that the antiferromagnetic skyrmion texture is found for different shapes of the lattice boundaries and the scale of the skyrmions in the bulk changes with the DMI strength. Then, we explore the quantum nature of the resulting ground states studying their entanglement entropy and concurrence.

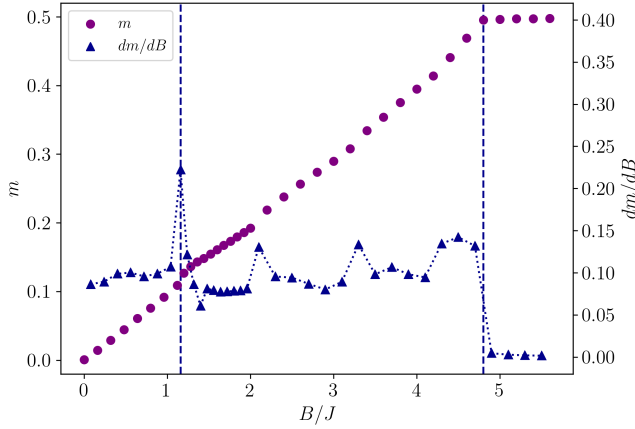


FIG. 2. Average magnetization per site  $m$  in the magnetic field direction (purple circles) and its derivative, the susceptibility (dark blue triangles), as a function of magnetic field  $B/J$ . As expected,  $m$  approaches the value  $1/2$  for high  $B/J$ . The susceptibility is discontinuous at  $B/J \simeq 1.16$  and  $B/J \simeq 4.8$  (dashed dark blue vertical lines).

### A. Magnetization

We begin our study by computing expectation values of local spin operators. Magnetization per site  $m = \left(\sum_{\mathbf{r}} \langle \hat{S}_{\mathbf{r}}^z \rangle\right) / N$  for each value of  $B/J$  is presented in Fig. 2. From now on, angle brackets  $\langle \rangle$  denote the expectation value of the corresponding operator (in this case, of  $\hat{S}^z$  at site  $\mathbf{r}$ ). As we can see, it reaches its maximum value ( $m = 1/2$ ) for high magnetic fields. This means that the system is field-polarized for  $B/J \gtrsim 4.8$ .

At plain sight,  $m$  seems to be continuous for the full range of  $B/J$ . To search for signatures of possible different phases, we compute its derivative (i.e. the magnetic susceptibility  $\frac{dm}{dB}$ ). Susceptibility shows a peak at  $B/J \simeq 1.16$  and a jump at  $B/J \simeq 4.8$ . This indicates that  $m$  has a single jump discontinuity around  $B/J \simeq 1.16$  unlike the ferromagnetic system, where clear jumps in  $m$  delimit the skyrmion region [19]. These changes in the behavior of  $\frac{dm}{dB}$  with  $B$  are signatures of the stabilization of different phases, as we confirm with other numerical results in the next subsections.

As we mentioned above, there seem to be three main regions demarcated by discontinuities in the susceptibility. We turn to the local magnetization of the ground states to check if this is the case. We show the real-space magnetization profiles of the system, i.e.  $\langle \hat{\mathbf{S}}_i \rangle \equiv (\langle \hat{S}_i^x \rangle, \langle \hat{S}_i^y \rangle, \langle \hat{S}_i^z \rangle)$  for each spin  $i$ , at different values of  $B/J$  in Fig. 3. The first and second components of  $\langle \hat{\mathbf{S}}_i \rangle$  are represented by arrows, and colors denote spin expectation values  $\langle \hat{S}_i^z \rangle$ .

The low field phase is depicted in panel (a) of Fig. 3: an antiferromagnetic helical phase formed by three interpenetrated helices, one in each triangular sublattice (A, B, C). The antiferromagnetic skyrmion phase formed by

three interpenetrated ferromagnetic skyrmion textures is shown in panel (b), corresponding to the intermediate field region. We notice however that the magnetization patterns found at higher field values of the intermediate region differ markedly from those of panel (b): panel (c) shows these patterns, which are non-trivial skyrmion-like textures similar to those found in the classical case [35]. We will further discuss this in the next subsection, where we analyze the scalar chirality. The third region, where  $m \simeq 1/2$  corresponds to the field-polarized phase, and is illustrated in panel (d).

### B. Scalar chirality

Scalar chirality is a commonly-used quantity that corresponds to  $N_{Sk}$  for a discrete lattice, and as such it signals the emergence of magnetic skyrmions in classical spin systems. On a triangular lattice, it is defined as

$$Q_{clas} = \frac{1}{8\pi} \sum_{(i,j,k) \in \Delta / \nabla} \mathbf{m}_i \cdot (\mathbf{m}_j \times \mathbf{m}_k), \quad (3)$$

addition where  $\mathbf{m}_i$ ,  $\mathbf{m}_j$  and  $\mathbf{m}_k$  are classical magnetic moments of unit length located at sites  $i$ ,  $j$  and  $k$  respectively. The sum runs over sites  $i$ ,  $j$  and  $k$  that form each non-overlapping triangular plaquette. Examples of spins  $i$ ,  $j$  and  $k$  on an upward triangular plaquette ( $\Delta$ ) and on a downward one ( $\nabla$ ) of the lattice are shown in Fig. 1. In what follows, we will apply a quantized version of the scalar chirality [15], given by

$$Q = \frac{1}{\pi} \sum_{(i,j,k) \in \Delta / \nabla} \langle \hat{\mathbf{S}}_i \cdot (\hat{\mathbf{S}}_j \times \hat{\mathbf{S}}_k) \rangle, \quad (4)$$

where the sum once again runs over sites  $i$ ,  $j$  and  $k$  that form an elementary triangular plaquette (see Fig. 1). We will refer to the quantum scalar chirality  $Q$  as quantum chirality or chirality interchangeably going forward.

Chirality as a function of magnetic field  $B/J$  is shown in Fig. 4. At first sight, we see that the chirality  $Q$  defines three main regions. At lower fields,  $Q$  is comparatively small and positive up to  $B/J \simeq 1.2$ . Then there is a range of magnetic field values in which  $Q$  is negative, and its absolute value  $|Q|$  is visibly higher than for lower fields, reaching its maximum value at  $B/J \simeq 2.6$ . Finally,  $|Q|$  decreases smoothly until it reaches 0 at  $B/J \simeq 4.8$ .

As was done for the magnetization  $m$ , we compare the magnetic susceptibility with the chirality  $Q$  in Fig. 4. As mentioned in the previous subsection, the magnetic susceptibility has a peak at  $B/J \simeq 1.16$  and a jump at  $B/J \simeq 4.8$ , both closely matching the changes in the sign of  $Q$ , and thus establishing three ranges of magnetic fields with different phases. At low magnetic fields ( $B/J \lesssim 1.2$ ), a perfect helical phase would have  $Q = 0$ , and this is actually the case for  $B/J = 0$ . However,  $|Q|$

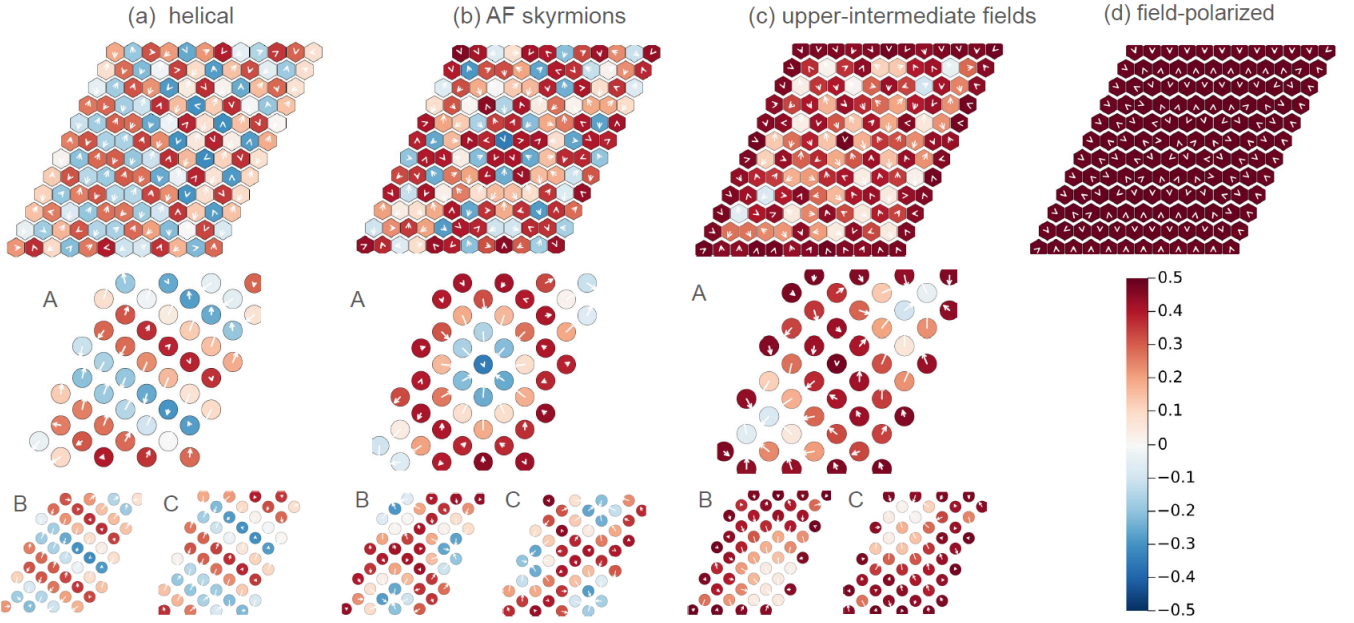


FIG. 3. Representative magnetization profiles for the obtained ground states: (a) AF helical phase at  $B/J = 0.8$ , (b) AF skyrmions at  $B/J = 1.76$ , (c) higher-field AF skyrmion-like phase at  $B/J = 3.4$ , and (d) field-polarized at  $B/J = 5.4$ . Local magnetization of the entire lattice for each phase is presented on the first row. For the first three cases, we also display the profiles for each triangular sublattice (A, B and C, as in Fig. 1). The colorbar indicates the  $\langle \hat{S}^z \rangle$  scale.

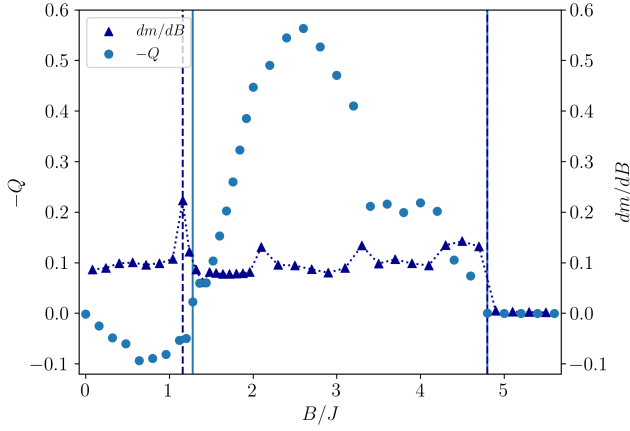


FIG. 4. Chirality  $Q$  (blue circles) and magnetic susceptibility (dark blue triangles) as a function of  $B/J$ . We multiply  $Q$  by  $-1$  so that  $Q$  and the susceptibility take mostly positive values, which allows for an easier comparison of changes in their behavior. Solid blue lines indicate  $B/J$  values where  $Q$  changes sign and dashed dark blue lines mark discontinuities in the susceptibility. Note that at higher fields both lines show up at  $B/J \simeq 4.8$ .

starts to increase with  $B/J$  as in the quantum ferromagnetic case [15] due to the OBC and quantum fluctuations. Most importantly,  $Q$  is clearly non-zero in the skyrmion region ( $1.2 \lesssim B/J \lesssim 4.8$ ), in agreement with the local magnetization patterns presented in Fig. 3. This  $Q$  region also exhibits two subregions: one where  $|Q|$

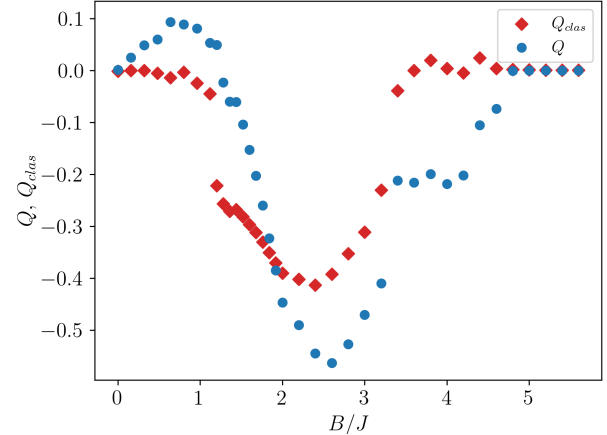


FIG. 5. Classical chirality  $Q_{\text{clas}}$  (red diamonds) and quantum chirality  $Q$  (blue circles) as a function of  $B/J$ .

is significantly higher ( $1.2 \lesssim B/J \lesssim 3.2$ ), corresponding to the antiferromagnetic skyrmion phase (Fig. 3(b)), and a higher-field sector ( $3.2 \lesssim B/J \lesssim 4.8$ ) where  $|Q|$  drops, signalling the intermediate skyrmion-like phases illustrated in Fig. 3(c). Finally, as expected,  $Q = 0$  for the field-polarized phase. Therefore, as in classical systems, and even in this antiferromagnetic case, the chirality serves as an order parameter to indicate non-trivial skyrmion textures.

We stated above that a change in sign of  $Q$  at lower

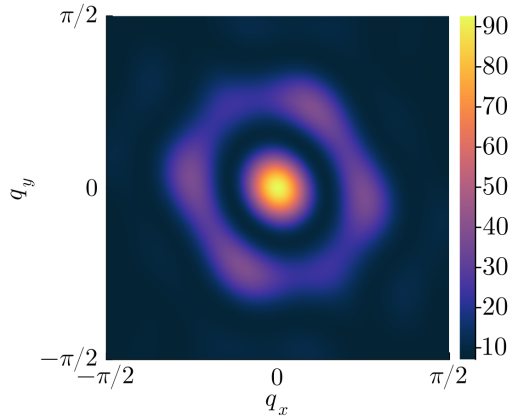


FIG. 6. Structure factor  $S_{zz}$  (in arbitrary units) of sublattice A from Fig. 3(b). It resembles  $S_{zz}$  of a lattice hosting a single quantum F skyrmion from Ref. [19].

magnetic fields can be a good indicator of the rise of skyrmions even if  $Q \approx 0$ . As a complement to this study, we compute  $Q_{clas}$  replacing each  $\mathbf{m}$  in Eq.(3) with  $\langle 2\hat{\mathbf{S}} \rangle$  as was done in previous works [16, 18]. Classical chirality  $Q_{clas}$  vs.  $B/J$  is presented in Fig. 5, along with  $Q$ . It can be seen that  $Q_{clas}$  is non-vanishing for  $1.2 \lesssim B/J \lesssim 3.2$  (region where ground states display skyrmion patterns in their local magnetization) and negligible elsewhere. Thus,  $Q_{clas}$  can be used to detect quantum skyrmions, whether ferromagnetic [16, 18] or antiferromagnetic. Moreover, both  $Q_{clas}$  and  $Q$  have a similar qualitative behavior but differ in the skyrmion-like region, where  $Q_{clas} \approx 0$  since spins are highly polarized. One open question is whether the value of  $Q$  is related to the stability of quantum AF skyrmions as in the ferromagnetic case [18]. This question will be addressed in future work.

Thus, chirality  $Q$  can be used to identify quantum AF skyrmions, as it was the case for quantum ferromagnetic skyrmions. However, contrary to what happens in the ferromagnetic case [13], quantum fluctuations suppress the lower-field chiral region with respect to the classical chirality diagram for this Hamiltonian from Ref. [25]. This is consistent with previous spin wave studies for these systems [25, 41].

### C. Structure factor

So far we have established that non-trivial magnetic spin textures emerge as ground states of the simple antiferromagnetic model introduced in Eq.(2) at intermediate magnetic fields. Based on their magnetization patterns and chirality, these chiral textures can be regarded to be antiferromagnetic skyrmion textures. In particular, the magnetization pattern of sublattice A from Fig. 3(b) resembles that of a quantum ferromagnetic skyrmion. We then resort to the spin-spin correlation function to check

if sublattice spins are also correlated with each other in the same way as spins from quantum ferromagnetic skyrmions. We compute the structure factor

$$\mathcal{S}_{\alpha\beta}(\mathbf{q}) = \sum_{\mathbf{r}, \mathbf{r}'} e^{i\mathbf{q}(\mathbf{r}-\mathbf{r}')} \langle \hat{S}_{\mathbf{r}}^{\alpha} \hat{S}_{\mathbf{r}'}^{\beta} \rangle,$$

which is the Fourier transform of the spin-spin correlation function between spins at positions  $\mathbf{r}$  and  $\mathbf{r}'$ , with  $\alpha, \beta = x, y, z$ . We are interested in the sublattice structure factor, so the sum in  $\mathcal{S}_{\alpha\beta}(\mathbf{q})$  runs over sites of the same sublattice.

Fig. 6 shows  $\mathcal{S}_{zz}$  of sublattice A of the ground state for  $B/J = 1.76$ . There is a Bragg peak at  $\mathbf{q} = 0$  due to the non-zero magnetization in the  $\hat{z}$  direction. We notice that the  $\mathcal{S}_{zz}$  of the sublattice resembles the  $\mathcal{S}_{zz}$  of a system hosting a single quantum ferromagnetic skyrmion [19]. This agrees with the three sublattice pattern found in the local magnetization (Fig. 3(b)) where, for this system size, a single ferromagnetic skyrmion pattern is realized in one of the sublattices.

### D. Robustness of the antiferromagnetic skyrmion phase

An important issue to address is the robustness of the antiferromagnetic skyrmion phase with the shape and size of the lattice, given that boundary effects are expected due to the reduced system size. In order to study this, we redid the calculations for a triangular lattice with hexagon boundaries. In Fig. 7(b) we show the resulting full lattice and sublattices textures for  $B/J = 1.76$  to compare them with Fig. 3(b). We can see that indeed there is a three-interpenetrated-sublattice antiferromagnetic skyrmion texture, and that the size of the sublattice skyrmions is roughly the same.

Moreover, to further explore the consistency of our calculations, we examine the local magnetization for other DMI values. These results are presented in Fig. 7(a) and (c). It is well known that, in the classical case, skyrmion radii depend on the  $D/J$  ratio: a larger (smaller)  $D/J$  implies smaller (larger) skyrmions [3]. This is also the case for these antiferromagnetic quantum skyrmions: larger skyrmions are found at  $D/J = 0.6$ ,  $B/J = 1.2$  (panel (a)) and smaller ones at  $D/J = 0.9$ ,  $B/J = 2.0$  (panel (c)).

Finally, in Fig. 8 we show that the antiferromagnetic skyrmion lattice is robust for larger system sizes, presenting the sublattice magnetization profiles for  $D/J = 0.8$ ,  $B/J = 1.76$  for  $L = 20$ . Due to the larger system size, the three-sublattice structure is more noticeable. Furthermore, the size of the individual skyrmions in each sublattice does not change significantly.

In summary, these analyses suggest that — despite some limitations due to the shape of the lattice, boundaries and system size — our findings described in previous subsections are robust, particularly those regarding quantum antiferromagnetic skyrmions.

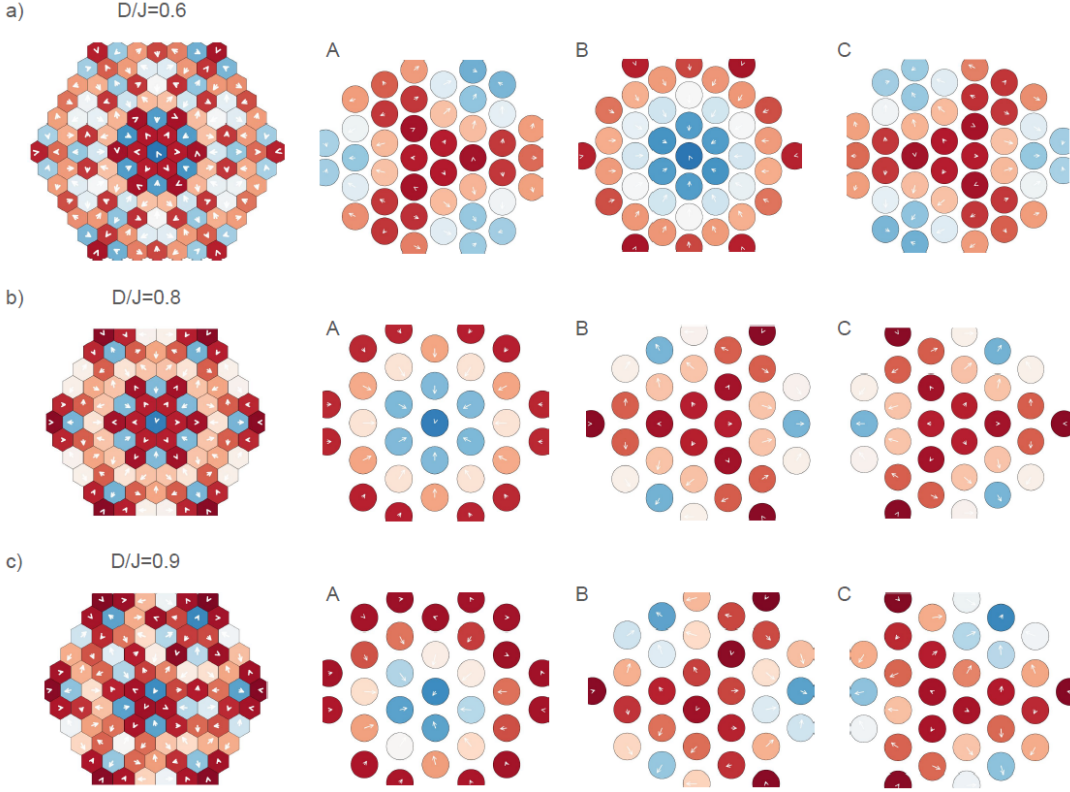


FIG. 7. Real-space magnetization per site of the ground states of Eq.(2) (first column) and for each of the three sublattices (from second to fourth column) for different values of  $D/J$  considering a disk-shaped triangular lattice. We take (a)  $D/J = 0.6$ ,  $B/J = 1.2$ , (b)  $D/J = 0.8$ ,  $B/J = 1.76$ , and (c)  $D/J = 0.9$ ,  $B/J = 2.0$ . Notice that panel (b) matches the parameter set from Fig. 3(b).

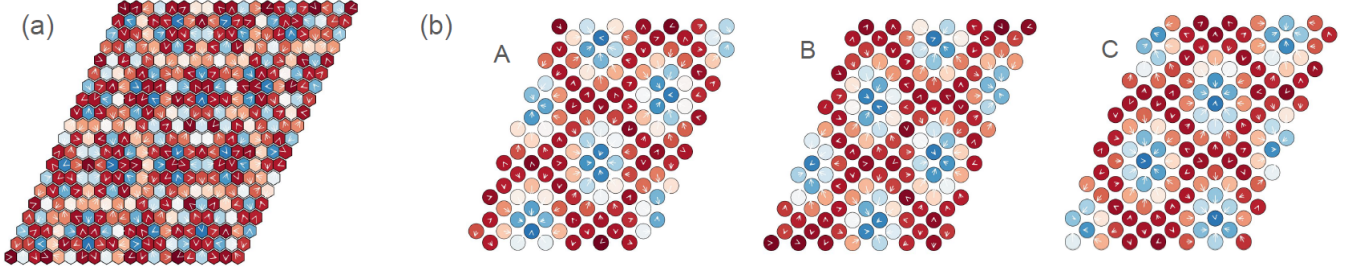


FIG. 8. Local magnetization for the total lattice (panel a) and each sublattice (panel b) of the ground state of Eq.(2) for  $B/J = 1.76$  and  $D/J = 0.8$  and considering a  $L = 20$  lattice.

### E. Quantum entanglement

The preceding subsections involved expectation values of quantities that have a classical counterpart. We will now focus on quantum entanglement, which has no classical analogue. Over the last decades, entanglement has become a fundamental tool to characterise condensed matter physics systems with strong correlations [42–46]. Here, we aim to use this quantity to inspect the quantumness of the obtained ground states. Since we are working with wavefunctions, which are pure states, we can use

the entanglement entropy

$$S_a = -\text{Tr}(\rho_a \log_2 \rho_a)$$

to study the entanglement between disjoint subsets  $a$  and  $b$  of the system ( $a \cup b$ ), where  $\rho_a = \text{Tr}_b \rho$  is the reduced density matrix of subsystem  $a$  obtained taking the partial trace over  $b$  of the density matrix  $\rho$  of the system. The density matrix  $\rho$  associated with a ground state  $|\psi\rangle$  is the projection operator given by  $\rho = |\psi\rangle\langle\psi|$ .

To calculate  $S_a$ , we split our 1D-mapping of the 2D system (see Appendix A) into two contiguous subsets labeled as subsystems  $a$  and  $b$ . In particular, we will take

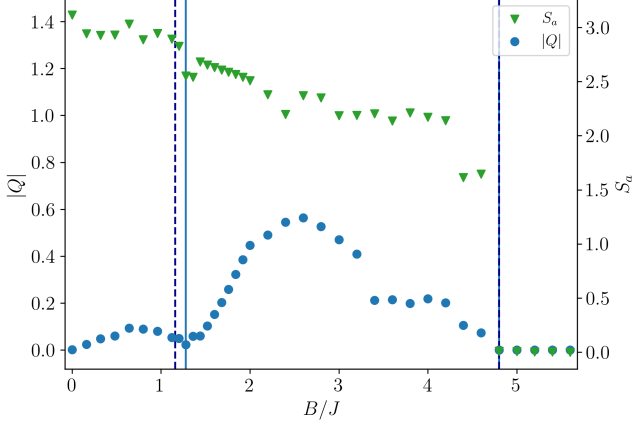


FIG. 9. Entanglement entropy  $S_a$  and rescaled chirality vs.  $B/J$ . Half-chain entanglement entropy (green triangles) was obtained considering each half of the system as subsystems  $a$  and  $b$ . Blue dots indicate  $|Q|$  for each  $B/J$ . Both quantities vanish for  $B/J \gtrsim 4.8$ . Solid vertical lines indicate where  $Q$  changes sign and dashed dark blue lines mark  $B/J$  values in which the magnetic susceptibility is discontinuous. Both lines coincide at  $B/J \simeq 4.8$ .

each equally-sized half of the system as subsystems  $a$  and  $b$ . The entanglement entropy  $S_a$  between each half of the system and for each value of  $B/J$  is presented in Fig. 9 along with a rescaling of  $Q$ . The entanglement entropy is non zero and almost constant at lower magnetic fields, drops to lower values at  $B/J \simeq 1.2$ , and becomes zero for  $B/J \gtrsim 4.8$ , which indicates that the ground state is a product state. This is consistent with the system being in a field-polarized phase at high magnetic fields. Moreover,  $S_a$  takes non-overlapping values in each of the three regions delimited with solid vertical lines, which are the same three main regions delimited by the chirality (see Section III B):  $B/J \lesssim 1.2$ , corresponding to AF helices, AF skyrmion and skyrmion-like textures in the  $1.2 \lesssim B/J \lesssim 4.8$  range, and a field-polarized ground state for  $B/J \gtrsim 4.8$ . Additionally, we see that  $S_a$  takes its highest values for the helical phase emerging at lower fields. This was also the case in the ferromagnetic system [19].

Based on these results, the entanglement entropy  $S_a$  changes in the different types of ground states in this system. Furthermore, we have shown it is clearly non-zero in the range of magnetic fields where topological textures are found, contributing to the quantum description of these ground states. In fact, in that region we also see there seem to be two subregions of  $S_a$ , in accordance to the two types of ground state textures at intermediate fields (Fig. 3(b) and (c)): AF skyrmions and a higher-field AF skyrmion-like texture, similar to that found in the classical system. If we take different left-right bipartitions of our system, we observe that  $S_a \sim 10^{-3}$  in the fully-polarized state for each choice of  $a$ , whereas  $S_a$  values are one order of magnitude larger for the AF

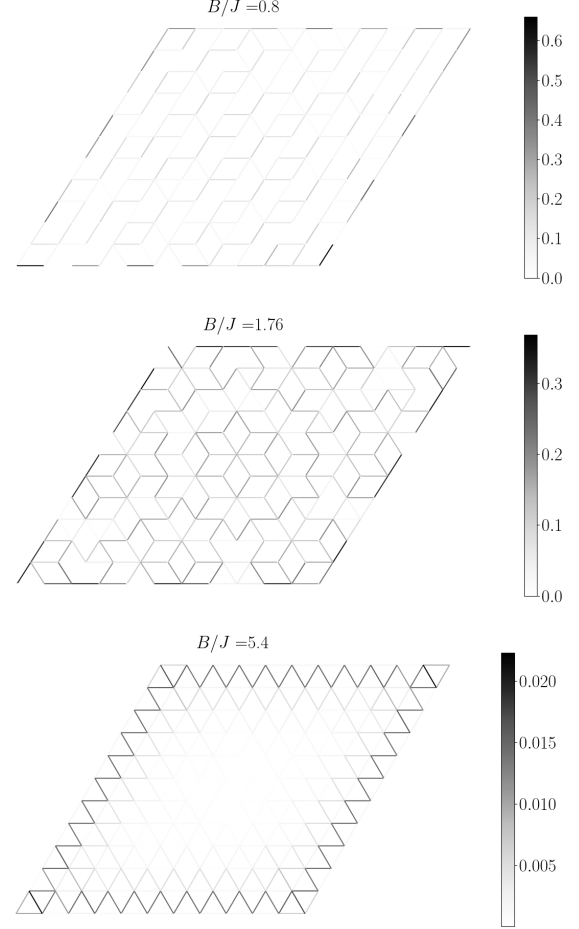


FIG. 10. Concurrence between nearest-neighbor spins for the helical phase at  $B/J = 0.8$  (top), the AF skyrmion lattice at  $B/J = 1.76$  (center) and fully-polarized phase at  $B/J = 5.4$  (bottom). Spin pairs involving at least one spin of the lattice boundary have the largest concurrences among all pairs in each phase considered.

skyrmion and helical phases.

So far we can conclude that there is entanglement in the AF skyrmion phase. In order to learn how this entanglement is distributed along the system, we employ the concurrence [47] between each pair of nearest-neighbor spins. To compute the concurrence  $C_{ij}$  between spins  $i$  and  $j$ , we first need the spin-flipped state

$$\tilde{\rho}_{ij} = (\sigma_y \otimes \sigma_y) \rho_{ij}^* (\sigma_y \otimes \sigma_y)$$

of the state  $\rho_{ij}$ , with  $\sigma_y$  the Pauli matrix  $y$  and  $\rho_{ij}^*$  the complex conjugate of the reduced density matrix of spins  $i$  and  $j$ . Then,  $C_{ij}$  is given by

$$C_{ij} = \max \left( 0, \sqrt{\lambda_1} - \sqrt{\lambda_2} - \sqrt{\lambda_3} - \sqrt{\lambda_4} \right),$$

where the  $\lambda_i$ 's are the eigenvalues of

$$R = \rho_{ij} \tilde{\rho}_{ij}$$

in decreasing order. Concurrence is such that  $0 \leq C_{ij} \leq 1$ , where  $C_{ij} = 0$  for separable states and  $C_{ij} = 1$  if the pair is maximally entangled (e.g. if the pair is in a Bell state).

Fig. 10 shows the concurrence between each pair of neighboring sites for different phases: AF helical, AF skyrmion and field-polarized. The AF helical texture displays the largest entanglement values of the three phases. Remarkably, in spite of this, the AF skyrmion phase has on average the largest nearest-neighbor concurrence. Concurrences of neighboring pairs of the field-polarized state practically vanish in the bulk and reach values that are at most one order of magnitude smaller than the other phases.

Considering all of the above, we can conclude that spins forming AF skyrmions are entangled, confirming the quantum nature of these ground states. Moreover, judging by the entanglement entropy  $S_a$ , entanglement seems to change as a function of the magnetic field in the three main regions defined by the magnetic susceptibility and the chirality. In particular, our results of the concurrence  $C_{ij}$  between spins  $i$  and  $j$  indicate that pair-wise entanglement notably differs in each of the main phases considered.

#### IV. Conclusions

We have presented a study of a simple skyrmion-hosting antiferromagnetic model in the triangular lattice, combining exchange interactions and in-plane DMI under an external magnetic field. Through DMRG calculations, we have studied the ground states of this spin-1/2 model, focusing on the characterization and robustness of the three-sublattice antiferromagnetic skyrmion phase.

Our numerical findings imply the stabilization of AF skyrmions formed by three interpenetrated sublattices in a finite range of magnetic fields. Variables such as the local magnetization and chirality show the stabilization of these textures, which are similar to those found in its classical counterpart. Even though the spin textures at intermediate magnetic fields are reminiscent of classical AF skyrmions, we found that there is entanglement present in these states, which proves their quantum nature. Most interestingly, this quantity also serves as a parameter to distinguish this phase from the low-field helices and the high-field polarized states.

In addition, we have checked the consistency of our calculations comparing results for different geometries of the (open) boundary conditions, and found that the AF skyrmion texture does not visibly change. We have seen that this is not a fine-tuned regime since these textures can be stabilized for different strengths of DMI as well, and the skyrmion size changes accordingly. Finally, although finite size effects are expected due to the computational limitations, we have seen that the AF skyrmion phase is present at larger systems sizes.

Given that one key feature of AF skyrmions is their

topological protection, it would be interesting to explore how robust quantum AF skyrmions are against external perturbations. AF skyrmions also present no skyrmion Hall effect [48–51] under certain conditions [52], which is of interest for technological applications, so a thorough study of the dynamics of quantum AF skyrmions would be pertinent. We leave both of these research avenues for future work.

#### Acknowledgments

I. C. would like to thank Mauricio Matera and Loic Herviou for insights and helpful discussions. The authors thank the Subsecretaría de Ciencia y Tecnología and the SNCAD from Argentina. I. C. also thanks the Laboratorio de Investigación y Formación en Informática Avanzada (UNLP-CICPBA, Argentina) for the computational resources. F. A. G. A. is partially supported by CONICET (PIP 2021-112200200101480CO, PIBAA 2872021010 0698CO), SECyT UNLP (PI+D X947 - X1065) and Agencia I+D+i (PICT-2020-SERIE A-03205). I. C., F. H. and L. R. are partially supported by SECyT UNLP (PI+D X943 - X1050). Part of the numerical simulations in this work were carried out using the Clementina XXI supercomputer from Argentina.

#### A. DMRG implementation and convergence

DMRG was introduced as a numerical approach to study one-dimensional quantum systems. Therefore, we must map each 2D lattice into a 1D chain to apply the MPS formulation of this algorithm. The goal is to choose a mapping in which a fair amount of the neighboring spins from the lattice are still nearest neighbors in the chain since the 2D-to-1D mapping inherently introduces long-ranged interactions in the resulting 1D model. In our case, we use a zigzag ordering as in Ref. [19]. An example of a triangular lattice mapped into a 1D chain using this ordering is presented in Fig. A.1.

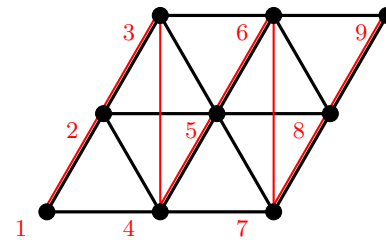


FIG. A.1. Triangular lattice (black lines) and its associated 1D chain (red lines).

In the DMRG calculations, we used a random MPS as initial state and performed a large number of sweeps at smaller bond dimensions  $\chi$  ( $\chi \leq 100$ ) to aid convergence. Then, we employed gradually larger values of  $\chi$

until reaching the preestablished maximum value. From that point onwards, sweeps continued until the relative energy difference between sweeps was smaller than  $10^{-7}$ . Taking into account that DMRG is a variational algorithm, we repeated several times the ground state simulations for each  $B/J$  and different values of  $\chi$ . Our results of the main text correspond to ground state approximations  $\psi(B)$  in which  $E$  and  $m$  change in less than 0.2% between subsequent  $\chi$ 's.

Since we are especially interested in the AF skyrmion phase, we check for convergence of several properties with respect to the bond dimension  $\chi$  for  $B/J = 1.76$ , where the ground state is a three-sublattice AF skyrmion tex-

ture. Due to the size of the system, we expect there to be boundary effects, especially in the chirality calculations, so in order to study the bulk chirality we did not include boundary sites in the computation of  $Q$ . In Fig. A.2 we plot the energy, magnetization and chirality of the ground state obtained for a  $L = 12$  system at  $B/J = 1.76$  as a function of the bond dimension  $\chi$ . In all three cases, we see that clearly the system converges to a finite value. Fitting the data with a simple hyperbolic function, we find that these quantities tend to  $E_{\chi \rightarrow \infty} = -109.50024(2)$ ,  $m_{\chi \rightarrow \infty} = 0.170500080(5)$  and  $Q_{\chi \rightarrow \infty} = -0.168346(9)$ , respectively.

---

[1] A. N. Bogdanov and D. A. Yablonskii, Thermodynamically stable vortexes in magnetically ordered crystals-mixed state of magnetics, *Zh. Eksp. Teor. Fiz.* **95** (1989).

[2] A. Bogdanov and A. Hubert, Thermodynamically stable magnetic vortex states in magnetic crystals, *Journal of Magnetism and Magnetic Materials* **138**, 255 (1994).

[3] N. Nagaosa and Y. Tokura, Topological properties and dynamics of magnetic skyrmions, *Nature Nanotechnology* **8**, 899 (2013).

[4] A. Fert, V. Cros, and J. Sampaio, Skyrmions on the track, *Nature Nanotechnology* **8**, 152 (2013).

[5] J. Sampaio, V. Cros, S. Rohart, A. Thiaville, and A. Fert, Nucleation, stability and current-induced motion of isolated magnetic skyrmions in nanostructures, *Nature Nanotechnology* **8**, 839 (2013).

[6] I. M. Börge Göbel and O. A. Tretiakov, Beyond skyrmions: Review and perspectives of alternative magnetic quasiparticles, *Physics Reports* **895**, 1 (2021).

[7] T. Okubo, S. Chung, and H. Kawamura, Multiple-q states and the skyrmion lattice of the triangular-lattice Heisenberg antiferromagnet under magnetic fields, *Phys. Rev. Lett.* **108**, 017206 (2012).

[8] A. O. Leonov and M. Mostovoy, Multiply periodic states and isolated skyrmions in an anisotropic frustrated magnet, *Nat. Commun.* **6**, 8275 (2015).

[9] D. Amoroso, P. Barone, and S. Picozzi, Spontaneous skyrmionic lattice from anisotropic symmetric exchange in a Ni-halide monolayer, *Nat. Commun.* **11**, 1 (2020).

[10] O. I. Utesov, Thermodynamically stable skyrmion lattice in a tetragonal frustrated antiferromagnet with dipolar interaction, *Phys. Rev. B* **103**, 064414 (2021).

[11] S. Mühlbauer, B. Binz, F. Jonietz, C. Pfleiderer, A. Rosch, A. Neubauer, R. Georgii, and P. Böni, Skyrmion lattice in a chiral magnet, *Science* **323**, 915 (2009).

[12] X. Yu, Y. Onose, N. Kanazawa, J. H. Park, J. Han, Y. Matsui, N. Nagaosa, and Y. Tokura, Real-space observation of a two-dimensional skyrmion crystal, *Nature* **465**, 901 (2010).

[13] A. Roldán-Molina, M. J. Santander, A. S. Nunez, and J. Fernández-Rossier, Quantum fluctuations stabilize skyrmion textures, *Phys. Rev. B* **92**, 245436 (2015).

[14] V. Lohani, C. Hickey, J. Masell, and A. Rosch, Quantum skyrmions in frustrated ferromagnets, *Phys. Rev. X* **9**, 041063 (2019).

[15] O. M. Sotnikov, V. V. Mazurenko, J. Colbois, F. Mila, M. I. Katsnelson, and E. A. Stepanov, Probing the topology of the quantum analog of a classical skyrmion, *Phys. Rev. B* **103**, L060404 (2021).

[16] A. Joshi, R. Peters, and T. Posske, Ground state properties of quantum skyrmions described by neural network quantum states, *Phys. Rev. B* **108**, 094410 (2023).

[17] A. Joshi, R. Peters, and T. Posske, Quantum skyrmion dynamics studied by neural network quantum states, *Phys. Rev. B* **110**, 104411 (2024).

[18] P. Siegl, E. Y. Vedmedenko, M. Stier, M. Thorwart, and T. Posske, Controlled creation of quantum skyrmions, *Phys. Rev. Res.* **4**, 023111 (2022).

[19] A. Haller, S. Groenendijk, A. Habibi, A. Michels, and T. L. Schmidt, Quantum skyrmion lattices in Heisenberg ferromagnets, *Phys. Rev. Res.* **4**, 043113 (2022).

[20] S. Gao, H. D. Rosales, F. A. Gómez Albarracín, V. Tsurkan, G. Kaur, T. Fennell, P. Steffens, M. Boehm, P. Čermák, A. Schneidewind, *et al.*, Fractional antiferromagnetic skyrmion lattice induced by anisotropic couplings, *Nature* **586**, 37 (2020).

[21] H. D. Rosales, F. A. Gómez Albarracín, K. Guratinder, V. Tsurkan, L. Prodan, E. Ressouche, and O. Zaharko, Anisotropy-driven response of the fractional antiferromagnetic skyrmion lattice in  $\text{MnSc}_2\text{S}_4$  to applied magnetic fields, *Phys. Rev. B* **105**, 224402 (2022).

[22] W. Legrand, D. Maccariello, F. Ajejas, S. Collin, A. Vecchiola, K. Bouzehouane, N. Reyren, V. Cros, and A. Fert, Room-temperature stabilization of antiferromagnetic skyrmions in synthetic antiferromagnets, *Nature Materials* **19**, 34 (2020).

[23] H. Jani, J.-C. Lin, J. Chen, J. Harrison, F. Maccherozzi, J. Schad, S. Prakash, C.-B. Eom, A. Ariando, T. Venkatesan, *et al.*, Antiferromagnetic half-skyrmions and bimerons at room temperature, *Nature* **590**, 74 (2021).

[24] T. Dohi, S. DuttaGupta, S. Fukami, and H. Ohno, Formation and current-induced motion of synthetic antiferromagnetic skyrmion bubbles, *Nat. Commun.* **10**, 1 (2019).

[25] S. A. Díaz, J. Klinovaja, and D. Loss, Topological magnons and edge states in antiferromagnetic skyrmion crystals, *Phys. Rev. Lett.* **122**, 187203 (2019).

[26] Z. Liu, M. d. Santos Dias, and S. Lounis, Theoretical investigation of antiferromagnetic skyrmions in a trian-

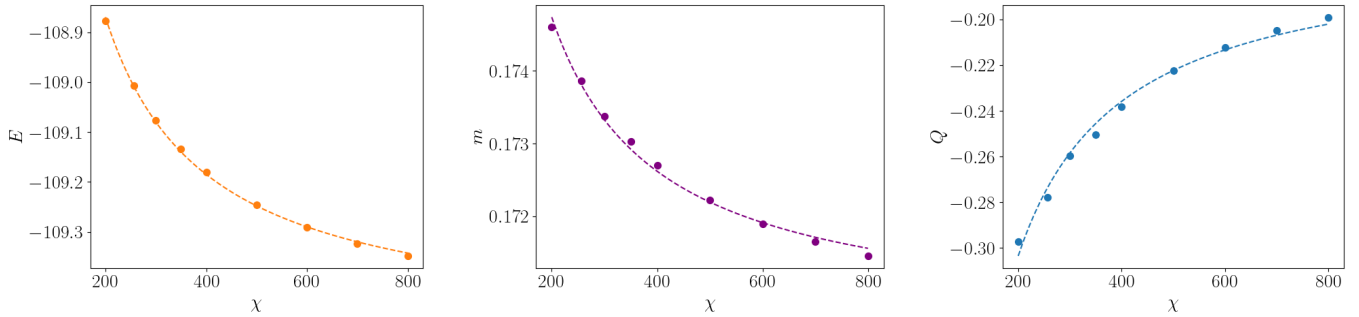


FIG. A.2. Energy (left), average magnetization per site (center) and chirality (right) vs bond dimension  $\chi$  of ground states of Eq.(2) for  $B/J = 1.76$ . The system hosts an AF skyrmion phase at this value of  $B/J$  as shown in Fig. 2.

gular monolayer, *Journal of Physics: Condensed Matter* **32**, 425801 (2020).

[27] S. R. White, Density matrix formulation for quantum renormalization groups, *Phys. Rev. Lett.* **69**, 2863 (1992).

[28] S. R. White, Density-matrix algorithms for quantum renormalization groups, *Phys. Rev. B* **48**, 10345 (1993).

[29] U. Schollwöck, The density-matrix renormalization group in the age of matrix product states, *Annals of Physics* **326**, 96 (2011), january 2011 Special Issue.

[30] S. R. White, Spin gaps in a frustrated Heisenberg model for  $\text{CaV}_4\text{O}_9$ , *Phys. Rev. Lett.* **77**, 3633 (1996).

[31] K. A. Hallberg, New trends in density matrix renormalization, *Advances in Physics* **55**, 477 (2006).

[32] E. Stoudenmire and S. R. White, Studying two-dimensional systems with the density matrix renormalization group, *Annual Review of Condensed Matter Physics* **3**, 111 (2012).

[33] R. Samajdar, W. W. Ho, H. Pichler, M. D. Lukin, and S. Sachdev, Quantum phases of Rydberg atoms on a kagome lattice, *Proceedings of the National Academy of Sciences* **118**, e2015785118 (2021), <https://www.pnas.org/doi/pdf/10.1073/pnas.2015785118>.

[34] D. Bhowmick, A. Haller, D. S. Kathiyat, T. L. Schmidt, and P. Sengupta, Quantum skyrmion liquid, *Phys. Rev. B* **111**, 134410 (2025).

[35] H. D. Rosales, D. C. Cabra, and P. Pujol, Three-sublattice skyrmion crystal in the antiferromagnetic triangular lattice, *Phys. Rev. B* **92**, 214439 (2015).

[36] M. Mohylna, J. Buša Jr, and M. Žukovič, Formation and growth of skyrmion crystal phase in a frustrated Heisenberg antiferromagnet with dzyaloshinskii-moriya interaction, *Journal of Magnetism and Magnetic Materials* **527**, 167755 (2021).

[37] M. Mohylna, F. A. Gómez Albarracín, M. Žukovič, and H. D. Rosales, Spontaneous antiferromagnetic skyrmion/antiskyrmion lattice and spiral spin-liquid states in the frustrated triangular lattice, *Phys. Rev. B* **106**, 224406 (2022).

[38] M. Mohylna and M. Žukovič, Stability of skyrmion crystal phase in antiferromagnetic triangular lattice with dmi and single-ion anisotropy, *Journal of Magnetism and Magnetic Materials* **546**, 168840 (2022).

[39] M. Mohylna, F. A. Gómez Albarracín, M. Žukovič, and H. D. Rosales, Frustration-driven topological textures on the honeycomb lattice: Antiferromagnetic meron-antimeron and skyrmion crystals emerging from spiral spin liquids, *Phys. Rev. B* **111**, 174435 (2025).

[40] M. Fishman, S. R. White, and E. M. Stoudenmire, The ITensor Software Library for Tensor Network Calculations, *SciPost Phys. Codebases* **4** (2022).

[41] M. Tomé, *Efecto de las fluctuaciones cuánticas en fases topológicas no triviales de la red triangular antiferromagnética*, Master's thesis, Universidad Nacional de La Plata (2019).

[42] H.-C. Jiang, Z. Wang, and L. Balents, Identifying topological order by entanglement entropy, *Nature Physics* **8**, 902 (2012).

[43] N. Laflorencie, Quantum entanglement in condensed matter systems, *Physics Reports* **646**, 1 (2016), quantum entanglement in condensed matter systems.

[44] B. Zeng, X. Chen, D.-L. Zhou, and X.-G. Wen, *Quantum Information Meets Quantum Matter* (Springer, 2019).

[45] S. Satoori, S. Mahdavifar, and J. Vahedi, Quantum correlations in the frustrated XY model on the honeycomb lattice, *Scientific reports* **13**, 16034 (2023).

[46] P. Laurell, A. Scheie, E. Dagotto, and D. A. Tennant, Witnessing entanglement and quantum correlations in condensed matter: A review, *Advanced Quantum Technologies* **8**, 2400196 (2024).

[47] W. K. Wootters, Entanglement of formation of an arbitrary state of two qubits, *Phys. Rev. Lett.* **80**, 2245 (1998).

[48] X. Zhang, Y. Zhou, and M. Ezawa, Magnetic bilayer-skyrmions without skyrmion Hall effect, *Nat. Commun.* **7**, 1 (2016).

[49] B. Göbel, A. Mook, J. Henk, and I. Mertig, Antiferromagnetic skyrmion crystals: Generation, topological Hall, and topological spin Hall effect, *Phys. Rev. B* **96**, 060406 (2017).

[50] S. Woo, K. M. Song, X. Zhang, Y. Zhou, M. Ezawa, X. Liu, S. Finizio, J. Raabe, N. J. Lee, S.-I. Kim, *et al.*, Current-driven dynamics and inhibition of the skyrmion Hall effect of ferrimagnetic skyrmions in GdFeCo films, *Nat. Commun.* **9**, 1 (2018).

[51] V. T. Pham, N. Sisodia, I. D. Manici, J. Urrestarazu-Larrañaga, K. Bairagi, J. Pelloux-Prayer, R. Guedas, L. D. Buda-Prejbeanu, S. Auffret, A. Locatelli, T. O. Menteş, S. Pizzini, P. Kumar, A. Finco, V. Jacques, G. Gaudin, and O. Boulle, Fast current-induced skyrmion motion in synthetic antiferromagnets, *Science* **384**, 307 (2024).

[52] A. Aldarawsheh, M. Sallermann, M. Abusaa, and S. Lounis, Current-driven dynamics of antiferromagnetic skyrmions: from skyrmion Hall effects to hybrid inter-

